Microphase Separation Controlled β-Sheet Crystallization Kinetics in Fibrous Proteins

Xiao Hu,[†,‡] Qiang Lu,[‡] David L. Kaplan,[‡] and Peggy Cebe*,[†]

Department of Physics and Astronomy, Department of Biomedical Engineering, Tufts University, Medford, Massachusetts 02155

Received November 5, 2008; Revised Manuscript Received January 14, 2009

ABSTRACT: Silk is a naturally occurring fibrous protein with a multiblock chain architecture. As such, it has many similarities with synthetic block copolymers, including the possibility for β-sheet crystallization restricted within the crystallizable blocks. The mechanism of isothermal crystallization kinetics of β-sheet crystals in silk multiblock fibrous proteins is reported in this study. Kinetics theories, such as Avrami analysis which was established for studies of synthetic polymer crystal growth, are for the first time extended to investigate protein self-assembly in β-sheet rich *Bombyx mori* silk fibroin samples, using time-resolved Fourier transform infrared spectroscopy (FTIR), differential scanning calorimetry (DSC) and synchrotron real-time wide-angle X-ray scattering (WAXS). The Avrami exponent, n, was close to 2 for all methods and crystallization temperatures, indicating formation of β-sheet crystals in silk proteins is different from the 3-D spherulitic crystal growth found in synthetic polymers. Observations by scanning electron microscopy support the view that the protein structures vary during the different stages of crystal growth, and show a microphase separation pattern after chymotrypsin enzyme biodegradation. We present a model to explain the crystallization of the multiblock silk fibroin protein, by analogy to block copolymers: crystallization of β-sheets occurs under conditions of geometrical restriction caused by phase separation of the crystallizable and uncrystallizable blocks. This crystallization model could be widely applicable in other proteins with multiblock (i.e., crystallizable and noncrystallizable) domains.

Introduction

Polymer crystallization controls the macroscopic structure and properties of long chain molecular materials.[1,2] The kinetics study of this process has provided a fruitful understanding of how polymer crystallization occurs.[1−5] Generally, the crystallization of polymers proceeds through several stages such as nucleation, lamellar growth, and growth of spherulitic aggregates.[1−6] This kinetic process can be described by well-known theories such as heuristic Avrami phase transition theory (also known as Kolmogorov−Johnson−Mehl−Avrami (KJMA) theory).[1−7] On the basis of the work of Avrami and others,[7−10] kinetic information like the growth rate of crystals can be obtained directly through the Avrami equation.[1−10] The growth geometry of crystals can also be predicted, in case of either one of two different nucleation mechanisms: predetermined nucleation, or sporadic nucleation.[1−10] Some experimental deviation from prediction by single instrumental methods, for instance, the Avrami exponent values are nonintegers or too high,[4,5] can also be reduced by comparing and analyzing data from different experimental methods. Although there are some limitations in this theory and corrections such as the Tobin equations[5] were proposed to improve its accuracy, it is still widely used as the major method to study the kinetics of different synthetic polymers and polymer blends. Direct observation by microscopy is then commonly used to test the prediction from this theory. In this way, polymer scientists can manipulate the process of crystallization in most synthetic macromolecules to obtain desired microstructures, including the size and density of spherulites.

Fibrous proteins are fundamentally a group of naturally occurring multiblock copolymers[11] containing crystallizable and uncrystallizable blocks. One of the most important structures in the formation of protein aggregates and fibrils comes from crystalline stacked β-pleated sheets.[11] Recent studies of small protein oligomers have revealed that the β-sheet core structure, which exists in most protein formations, plays a critical role in their folding and unfolding.[12−14] It is believed that these hydrophobic β-sheet regions may constitute the nucleation sites for protein folding. The unfolding process, therefore, will relate to the relaxation of these core structures at the end stage of the unfolding pathway, which was also observed to be the most resistant step to thermal unfolding. However, it is very difficult to observe the crystallization kinetic processes of β-sheet crystals directly. The size of fibrous protein crystals tends to be very small (~10 nm[11,15,16]) compared to most synthetic polymer crystal aggregates such as spherulites, and this often results in low contrast and extreme electron beam sensitivity for protein crystals. The growth mechanism of β-sheet crystals in multiblock proteins may also be different from the spherulite crystals formed in most synthetic homopolymers. Therefore, traditional methods like polarized microscopy (POM) used to observe polymer crystal growth kinetics cannot readily be applied to β-sheet crystals due to the size differences.

In this paper, we use for the first time traditional polymer crystallization kinetics theory to study the thermal crystallization of β-sheets in fibrous proteins. We use a pure β-sheet forming fibrous protein—*Bombyx mori* silk fibroin—as the experimental model example in this study. Silk fibroin is the structural protein that comprises the core material in spun silk fibers, and is dominated by the repeat amino acid primary sequence (Gly-Ala-Gly-Ala-Gly-Ser)$_n$ in the fibroin heavy chain.[11,15,17] During the fiber spinning process from the silkworm gland, the water soluble silk fibroin protein rapidly transforms to an insoluble fiber which contains about 55% antiparallel β-sheet crystals.[11,15,16] This amazing transition, coupled with the sequence chemistry in the protein chains, results in silk fibers with remarkable mechanical properties and lead to the widespread use of these fibers in the textile industry for thousands of years. In addition, as a pure biodegradable protein, new importance for this system is being realized in biomedical engineering, regenerative medicine, and drug release applications.[18−21] The

---

* Corresponding author. E-mail: peggy.cebe@tufts.edu.

[†] Department of Physics and Astronomy, Tufts University.

[‡] Department of Biomedical Engineering, Tufts University.

10.1021/ma802481p CCC: $40.75

mechanical, thermal, optical and degradation properties of silk fibroin in materials all relate to the formation of the β-sheet crystals.[11,18,22−26]

In a recent study,[24] we reported that silk fibroin follows an analogous crystallization mechanism to that proposed for melt crystallized synthetic polymers.[27,28] It is believed that a precursor structure exists in the beginning stage of β-sheet aggregation. With the help of the internal bound water molecules, a precursor structure is formed in the plasticized silk (having lower T_g near 80 °C) which promotes the crystallization of the β-sheet structures when the temperature increases above the glass transition temperature of fully dried silk (T_g = 178 °C).[22] In this study, we show how this important multiblock crystalline structure in fibrous protein assembles and grows to become the hydrophobic crystal that is the well-known antiparallel β-pleated sheet.

Experimental Section

Materials. The silk fibroin preparation process has been reported previously.[22−24] Briefly, *B. mori* silkworm cocoons were boiled in a Na_2CO_3 solution to extract the sericin.[11] The remaining crystallized silk fibroin was dissolved in LiBr solution at 60 °C, and then dialyzed against distilled water multiple times to remove the LiBr. After centrifugation and filtration, the final 2 wt % silk fibroin aqueous solution was cast to generate the uncrystalline silk fibroin films (around 10−20 μm thick).

FTIR Analysis. The detailed process was reported in our previous work.[24] Briefly, the silk fibroin samples were placed in a hot stage (Mettler, FP90) under the FTIR microscopic spectrometer (Bruker Equinox 55/S). The analysis was performed in transmission mode. The heating program for the hot stage was set up to control the temperature simultaneously when the IR spectra were recorded. During the FTIR analysis, the dried film samples were heated to different crystallization temperatures in the hotstage, and held until isothermal crystallization was completed. For each measurement, 32 scans were coadded with a nominal resolution of 4 cm^{-1} ranging from 400 to 4000 cm^{-1}. Fourier self-deconvolution (FSD), and detailed curve fitting process were used to determine the fraction of the secondary structure elements.[22−24]

Thermal Analysis. Samples with a mass of about 8 mg were sealed in Al pans and heated in a TA Q100 DSC, which was purged with a dry nitrogen gas flow of 50 mL/min.[29,30] The silk fibroin was treated using “cold” crystallization; i.e., the noncrystalline conformation films were heated to a temperature above their glass transition temperature (T_g(silk) = 178 °C), at which point the molecules gain sufficient mobility for the formation of the crystalline β-pleated sheets.

Standard mode DSC measurements were performed by heating at a fast rate from room temperature to the isothermal crystallization temperature, T_c, which ranged from 192−203 °C, to avoid unnecessary crystallization before T_c. Samples were maintained at T_c for a certain time (250−300 min) until crystallization was completed and no more exothermic heat flow could be observed at this temperature.

X-ray Scattering Analysis. Time-resolved wide-angle X-ray scattering (WAXS) experiments were conducted at Brookhaven National Laboratory (BNL), National Synchrotron Light Source (NSLS) beam line X27C with a wavelength of $\lambda = 0.1371$ nm. WAXS data were collected on a Braun one-dimensional microgap gas-filled wire detector. Sodelite and silicon standard reference powders were used to calibrate the q-vector ($q = 4\pi(\sin\theta)/\lambda$, for θ the half-scattering angle) for the angular range from $2\theta = 5°−35°$. The samples were heated quickly from T_g to T_c (10−15 s), and the X-ray intensity was then collected at T_c every minute until end of the crystallization at this temperature. The crystallization temperature ranged from 205−215 °C for WAXS studies. The intensity data were corrected for sample absorption, changes in incident beam intensity, and Kapton tape background. The scattering invariant, Q, is obtained from the total integrated area under the Lorentz-corrected intensity, $I(q)q^2$ curve:[31]

$$Q = \int I_{corr}(q)q^2\,\mathrm{d}q \tag{1}$$

where I_{corr} is the scattered intensity after all corrections have been applied. No small-angle X-ray scattering patterns were observed in any of the silk fibroin samples.

Scanning Electron Microscopy (SEM). The surface morphologies of the different silk films were imaged using a Zeiss Supra 55 VP SEM. Films were first fractured in liquid nitrogen and sputtered with platinum. The cross-sectioned pieces were imaged.

Enzyme Treatment. Chymotrypsin (obtained from Sigma Corp.), a proteolytic enzyme synthesized in the pancreas, was mixed with the PBS (sodium phosphate buffer) solution to obtain a chymotrypsin PBS solution (3.1 U/mL). Then the selected crystallized silk fibroin samples were immersed into the chymotrypsin PBS solution and kept in a 37 °C thermal environment for 24 h. After that, the biodegraded samples were washed with distilled water to completely remove the enzyme and PBS residues and dried in the vacuum for further study.

Results

FTIR Studies of Isothermal Crystallization. The isothermal crystallization kinetics of the silk fibroin was first studied by time-resolved FTIR. The silk film samples were first treated in the hot stage to remove bound water,[23,24] and then immediately jumped to the isothermal crystallization temperatures between 199 and 215 °C (listed in Table 1), which is above the T_g and below the starting point of degradation.

Figure 1 shows a typical real time FTIR spectrum during isothermal crystallization at 199 °C. The Amide I (1600−1700 cm^{-1}) region was selected to monitor the formation of the β-sheet crystals. At the starting time, the sample was in the noncrystalline state, and there was no peak observed in the wavenumber region of 1600−1640 cm^{-1}, which includes the main absorbance of β-sheet peaks in the Amide I region.[22,24,32] As the crystallization time increased, the β-sheet crystal peak appeared gradually, centered at 1625 cm^{-1}, and the random coil and α helix peak (centered at 1650 cm^{-1}) decreased simultaneously. Noncrystalline random coil and α helix structures were transformed into β-sheet crystals during isothermal crystallization. This result was similar with our previous work in comparing samples with different crystallinities.[22] The noncrystalline turn structure absorbance (centered at 1670−1690 cm^{-1}) was stable or only slightly decreased in this process and no obvious transition or band shift was observed. The increase in the β-sheet peak slowed down and stopped increasing after isothermal crystallization at 199 °C, indicating that the maximum crystallization ability of silk fibroin was reached at this temperature. Other samples isothermally crystallized at different temperatures between 199 and 215 °C all had the same features described above.

The intensity (area or height) changes of the crystal vibrational band have been utilized to monitor the crystallization kinetics of polymer materials.[33−35] A noncrystalline spectrum in the Amide I region was first recorded at the starting time at a certain crystallization temperature. An obvious growth of the β-sheet crystal peak at 1625 cm^{-1} was observed arising from the original spectrum. The area difference in the absorbance spectrum (ΔA) between 1600 and 1644 cm^{-1} was due to the absorbance intensity corresponding to the β-sheet crystals. When the crystallization time reached the critical crystallization point, for example, 35 min at 199 °C, the isothermal crystallization stopped for this temperature, and ΔA remained stable after this time. Therefore, we defined this maximum ΔA as the final ΔA_∞ for each particular isothermal crystallization temperature. The relative crystallinity, $X_c^{rel}(t)$, at different temperatures is therefore obtained as:

Table 1. Parameters Characterizing Isothermal β-Sheet Crystallization of *B. mori* Silk Fibroin: Avrami Rate Constant and Exponent, Half-Time, and Time to Maximum Rate of Change of Crystallinity

T_c (°C)	log K (±0.05)	n (±0.05)	$t_{1/2}$ (min, ± 0.1)[a]	t_i (min, ± 0.1)[b]
190.6[c]	−3.18	1.95	35.4	28.8
192.1[c]	−3.41	1.90	51.1	39.8
193.7[c]	−3.16	1.90	38.0	29.6
193.8[c]	−3.11	1.77	46.4	31.9
194.9[c]	−3.01	1.97	28.0	23.2
196.9[c]	−2.72	1.94	21.0	16.9
199.0[c]	−2.35	1.88	14.6	11.9
199.0[d]	−2.63	2.12	14.6	12.9
202.0[d]	−1.65	1.54	9.3	6.0
202.3[c]	−1.90	1.94	7.9	6.6
202.8[c]	−1.88	1.92	7.9	6.5
205.0[d]	−1.59	1.78	6.4	4.9
205.0[e]	−1.67	1.81	6.8	5.4
210.0[d]	−1.26	1.70	4.4	3.3
210.0[e]	−1.32	1.68	4.9	3.6
215.0[d]	−1.15	2.00	3.1	2.7
215.0[e]	−0.92	1.57	3.1	2.0

[a] Determined from eq 8 [b] Determined from eq 9 [c] Determined from DSC thermal analysis [d] Determined from FTIR analysis [e] Determined from X-ray scattering analysis

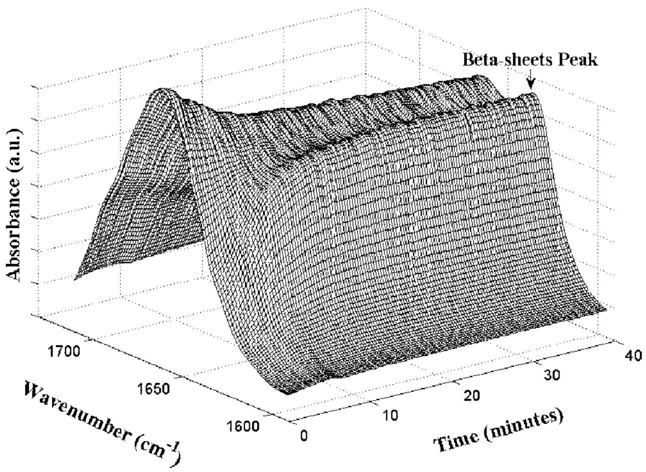

Figure 1. FTIR spectra during isothermal crystallization of silk fibroin at 199 °C. The Amide I (1600−1700 cm^{-1}) region was used to monitor formation of β-sheet crystals.

$$X_c^{\mathrm{rel}}(t) = \Delta A_t/\Delta A_\infty \tag{2}$$

where ΔA_t is area at time t. The ratio of ΔA_t to ΔA_∞ from the 1625 cm^{-1} crystal peak has a direct linear relation with the relative crystallinity.[35] In addition, Chen et al.[36,37] showed that the 1696 cm^{-1} crystal peak had the same crystallization kinetics as the 1625 cm^{-1} crystal peak in their study of spider silk crystallized by methanol treatment.

Figure 3 (and Figure 5) show relative crystallinity vs crystallization time calculated from the real-time FTIR spectra for the isothermal crystallization temperatures 199 °C (solid points) (Figure 3) and 205 (filled triangles), 210 (filled squares), and 215 °C (filled circles) (Figure 5). Detailed explanation and analysis will be described in the following sections.

In our previous work,[22] we used Fourier self deconvolution of the FTIR spectra to measure the absolute degree of crystallinity in isothermally crystallized fibroin. The β-sheet crystallinity ranged from 0.30 to 0.43 for samples isothermally crystallized in the temperature range from 199 to 214 °C, which covers most of the temperature range used in this work.

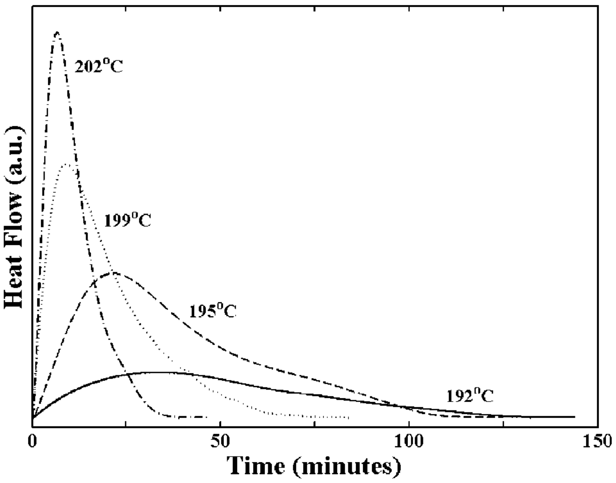

Figure 2. Isothermal crystallization kinetics of silk fibroin investigated by standard DSC. The exothermic heat flow, *H*(*t*), as a function of time, t, at four selected temperatures: 192, 195, 199, and 202 °C.

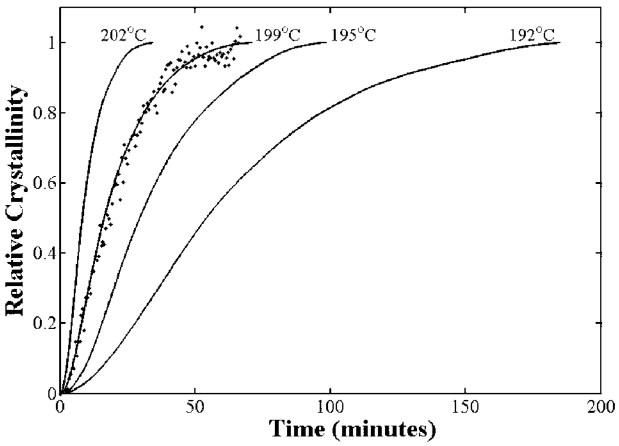

Figure 3. Relative crystallinity vs crystallization time for silk fibroin calculated from DSC (solid lines) and the real-time FTIR (points) for the isothermal crystallization temperatures 192, 195, 199, and 202 °C.

DSC Studies of Isothermal Crystallization. The isothermal crystallization kinetics was investigated using standard DSC performed in the range of crystallization temperatures T_c from 192 up to 202 °C. Figure 2 shows the exothermic heat flow, *H*(*t*), as a function of time, *t*, at four selected temperatures. The asymmetric shapes of the isothermal peaks suggest that this process contains secondary crystallization in the later stages of crystal growth.[1,4,5] Crystallization stops after a time about three to five times longer than the time to maximum heat flow, when no more exothermic heat flow can be detected.

The relative degree of crystallinity (X_c^{rel}) as a function of time was obtained from the integrated and normalized heat flow, using:[38,39]

$$X_c^{\mathrm{rel}}(t) = H(t)/H(\infty) = [\int_0^t \mathrm{d}t\,(\mathrm{d}H(t)/\mathrm{d}t)]/[\int_0^\infty \mathrm{d}t\,(\mathrm{d}H(t)/\mathrm{d}t)] \tag{3}$$

where $X_c^{\mathrm{rel}}(t)$ is the ratio of heat generated at time *t*, *H*(*t*), to the entire heat generated during crystallization, *H*(∞). Figure 3 (solid lines) shows the time dependence of the DSC relative crystallinity. The curves have approximately the same sigmoidal shape, indicating that the crystallization proceeds by a similar process at the different crystallization temperatures. In addition, relative crystallinity from the real-time FTIR study (point symbols) is also shown on the same scale. Comparison results show that the isothermal crystallization kinetics measured by these two distinct methods have very similar time dependence.

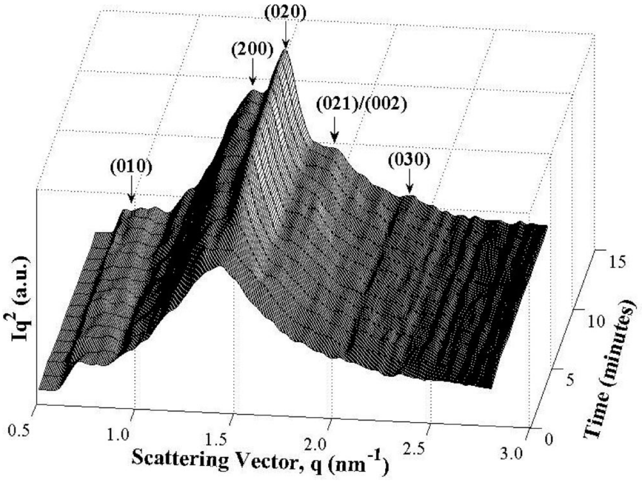

Figure 4. Temporal development of the wide-angle X-ray scattering pattern for silk fibroin crystallized at 215 °C, forming β-sheets crystal peaks (silk II), with d-spacings and Miller indices at 0.882 nm (010), 0.471 nm (200), 0.432 nm (020), 0.372 nm (021)/(002), 0.306 nm (030), as marked.[40,63]

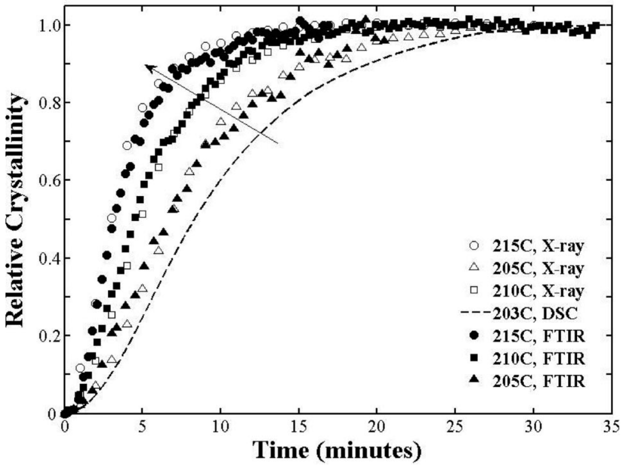

Figure 5. Relative crystallinity vs crystallization time of silk fibroin, from X-ray (open symbols) and from real-time FTIR (filled symbols) for isothermal crystallization temperatures 205 °C (triangles), 210 °C (squares), and 215 °C (circles). Results from DSC (dashed lines) at 203 °C are also shown. The arrow indicates the direction of increasing crystallization temperature.

X-ray Studies of Isothermal Crystallization. Real-time X-ray scattering experiments were performed at $T_c = 205$, 210, and 215 °C, and compared with the kinetic data obtained from real-time FTIR and DSC studies. Figure 4 shows the temporal development of the wide-angle X-ray scattering pattern for a sample crystallized at 215 °C. The baseline was corrected and the intensities were smoothed using a five point area-preserving binomial smoothing algorithm.

The amorphous pattern is the first scan of the sequence. Several crystal peaks can be observed to grow from the amorphous baseline as isothermal crystallization time increases, and they were identified to be from β-sheets (silk II), with d-spacings at 0.882 nm (010), 0.471 nm (200), 0.432 nm (020), 0.372 nm (021)/(002), 0.306 nm (030), with Miller indices as marked in Figure 4.[40] Q_a, the amorphous baseline area at $t = 0$, and $Q_c(t)$, the time dependent crystalline area, were determined from[31,41−43]

$$Q_a = \int I_a q^2 \, dq \qquad (4)$$

$$Q_c(t) = Q(t) - Q_a \qquad (5)$$

where I_a is the intensity of the amorphous peak, and $Q(t)$ is calculated from equation (1). For well crystallized samples, WAXS can be used to determine the crystallinity index at the end of crystallization (ratio of crystal peak area to total coherent scattering, Q_c/Q, at $t \to \infty$), although it tends to be lower than the absolute crystallinity in silk fibroin determined from either FTIR or DSC heat capacity.[22] We find WAXS crystallinity indices of 0.25 for 205 °C, 0.31 for 210 °C, and 0.33 for 215 °C.

The time-dependent relative WAXS crystallinity, $X_c^{rel}(t)$, is defined by normalizing the crystallinity to its value at long times:[44]

$$X_c^{rel}(t) = Q_c(t)/Q_c(t \to \infty) \qquad (6)$$

where $Q_c(t \to \infty)$ is the limiting value of WAXS crystallinity index reached after the completion of crystallization. The time development of relative crystallinity is shown in Figure 5 for $T_c = 205$ (open triangles), 210 (open squares), and 215 °C (open circles). At every point, the vertical height of the symbols covers the error bar which indicates the possible variation in relative crystallinity brought about by the effects of the normalization in WAXS pattern scaling. Since the intensity data are taken over one-minute time intervals, the error bars on the abscissa (which are not shown) will be of width equal to one minute. Included for comparison in Figure 5 is the DSC relative crystallinity, for data taken at $T_c = 203$ °C (dashed curve, without symbols). Figure 5 also includes data from the real-time FTIR study for these three isothermal crystallization temperatures (in filled symbols). These kinetics data points obtained from FTIR study are close to the curves obtained from WAXS, with at most, a ±5.7% difference between each data set. This indicates that in the high temperature region, in which crystallization occurs very quickly, the kinetic data from two different methods are consistent with each other.

Avrami Analysis of Crystallization Kinetics. The basic theory to describe the kinetics of isothermal crystallization is the Avrami equation:[1,2,8−10]

$$X_c^{rel}(t) = 1 - \exp(-Kt^n) \qquad (7)$$

where $X_c^{rel}(t)$ is the relative crystallinity of the crystallizing sample at different time t, K is the crystallization rate coefficient relating to the crystal growth geometry and the crystallization temperature, and n is the Avrami exponent parameter relating to the nucleation mechanism and crystal growth geometry.[1] K and n were determined from the intercept and slope, respectively, of the plot of $\log[-\ln(1 - X_c^{rel})]$ vs $\log(t)$ from the linear region of the plot. The normalized crystallinity from FTIR was then analyzed using the Avrami equation. Figure 6a shows the double-logarithmic plot from FTIR for the samples crystallized at $T_c = 215$, 210, 205, 202, and 199 °C. The n and log K values of the Avrami parameters from the FTIR kinetics study are summarized in Table 1.

Figure 6b shows the double logarithmic plots for crystallization from 192 to 202 °C from DSC kinetic data. For the ordinate range up to about 0, the curves are very linear. At very low times, only two curves (202 and 199 °C) have slight departure from linearity due to uncertainty in the starting time of crystallization. The double log plot tends to exaggerate the error at low times. Above ordinate values of zero, the curves all show a tendency to roll off to lower slope, as the secondary processes

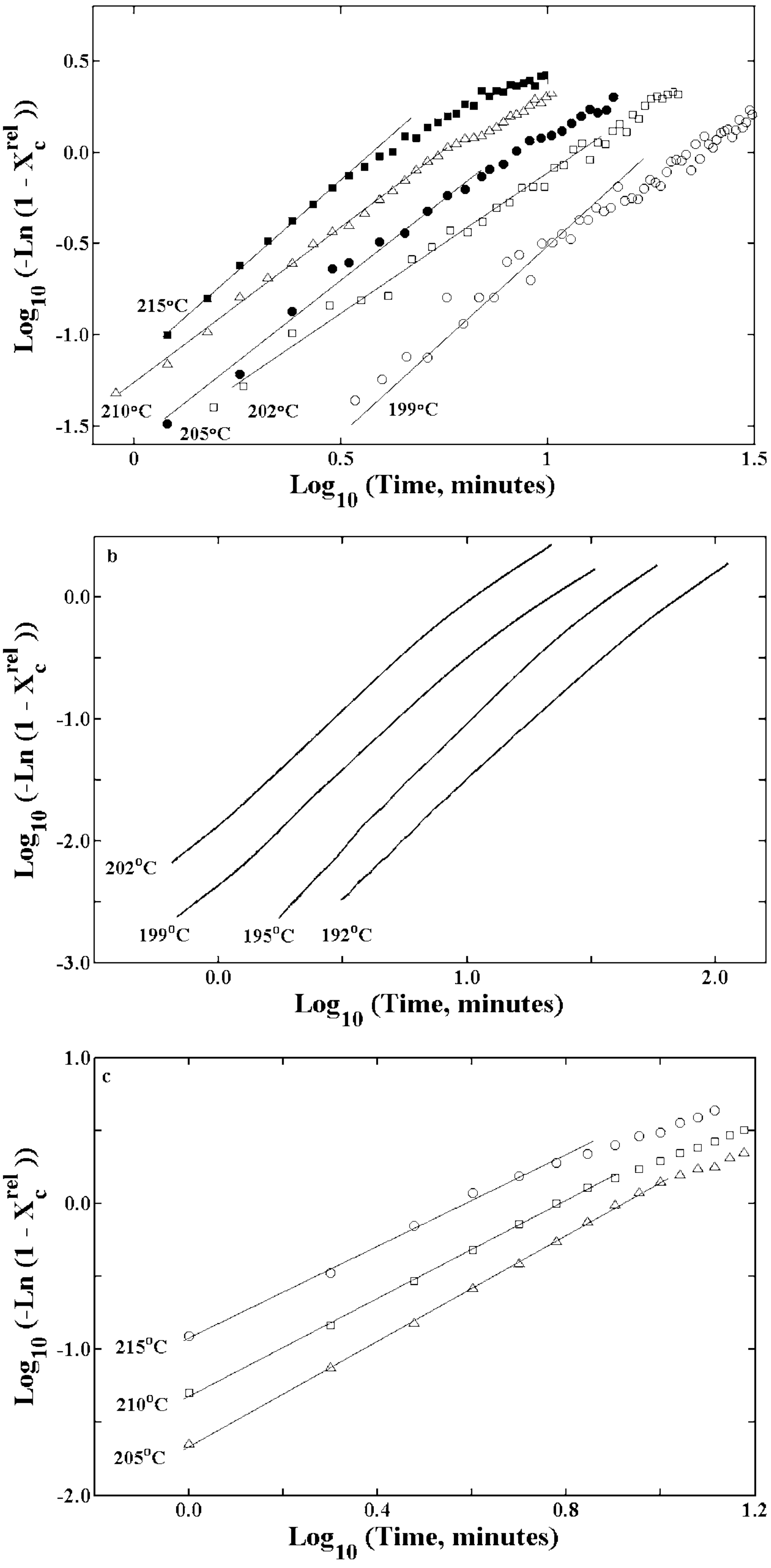

Figure 6. Isothermal crystallization kinetics of silk fibroin analyzed using the double-logarithmic Avrami equation: (a) from FTIR for samples crystallized at 199 (open circles), 202 (open squares), 205 (filled circles), 210 (open triangles), and 215 °C (filled squares); (b) from DSC for samples crystallized at 192, 195, 199, and 202 °C; (c) from X-ray for samples crystallized at 205 (filled triangles), 210 (open squares), and 215 °C (filled circles). The lines in parts a and c are fits of the data to the Avrami equation.

that slow crystallization begin to take over. The linear region of the curves was used to determine the Avrami rate coefficient, K and exponent, n, listed in Table 1.

Figure 6c shows the double-logarithmic plot for the samples crystallized at $T_c = 215$ °C, 210 °C, and 205 °C from X-ray kinetics data. The values of the Avrami parameters, n and K, from the WAXS kinetics study are summarized in Table 1. For all experiments, the Avrami exponent maintains a value between 1.54 and 2.12, with most values around 1.9. The crystallization rate coefficient, K, decreases with an increase of T_c.

Two characteristic times are also listed in Table 1. First is the crystallization half-time, $t_{1/2}$, the time at which the relative β-sheet content has reached 0.5. From n and K we can deduce $t_{1/2}$ from:[1]

$$t_{1/2} = ((\ln 2)/K)^{1/n} \tag{8}$$

β-sheet formation half-time, listed in the penultimate column of Table 1, decreases rapidly as the crystallization temperature increases. A second characteristic time is t_i, the time at which the rates of change (in heat flow, absorbance, or X-ray area) reach a maximum. Since t_i is the solution of $d^2X^{rel}/dt^2 = 0$, we can write t_i in terms of K and n, obtaining:

$$t_i = ((n - 1)/nK)^{1/n} \tag{9}$$

Calculated values of t_i are listed in the last column of Table 1. As a result of the asymmetry in the heat flow curves, we find that t_i is always less than $t_{1/2}$, and the degree of difference between the two times indicates the asymmetry is greatest at the lowest crystallization temperatures.

FTIR, DSC and WAXS kinetics data are combined to determine the crystallization growth rate, G, over the crystallization temperature range from 190 to 215 °C. The growth rate is related to the Avrami parameters, K and n, by $G \sim K^{1/n}$. In crystallization of semicrystalline synthetic polymers, G has the meaning of a linear growth rate, which can be compared to the data derived from measurements of spherulite diameter.[1-5] Here, for silk fibroin, no parallel microstructural features are seen: the β-pleated sheets do not form obvious spherulites or other large structures that can be seen by optical microscopy. The meaning of G in our case is the rate of conversion of fibroin noncrystalline structures (helices and random coils[22]) into more ordered sequences of pleated β-sheets. The growth direction is suggested to be along the rod direction, in the structural model presented by Krejchi.[45] It was suggested that regular chain folded architecture, similar to chain folded synthetic polymer lamellae, was applicable to a series of model periodic polypeptides. The crystal structure of the model materials was found to be similar to that reported for *B. mori* silk fibroin. These authors[45] construct an orthorhombic crystal model structure in which the crystal entity is roughly a square cross-sectioned rod, with the rod length (crystallographic a-axis) parallel to hydrogen bonding direction of the β-sheets. Therefore, we can obtain the growth rate of β-pleated sheets vs crystallization temperature from combined DSC, FTIR, and X-ray studies. The growth rate generally increases at higher T_c for *B. mori* silk fibroin β-sheets over the crystallization temperature range, from just above the glass transition temperature to a point just below the degradation temperature.

When the kinetic data for the growth rate were plotted in the form of an Arrhenius relationship (G vs 1/T, not shown for the sake of brevity), the resulting plot was nonlinear. Therefore, we model the growth rate using a transport function of the form[46]

$$G = G_0 \exp[-(U/R)/(T - T_0)] \tag{10}$$

where U is the transport activation energy, R is the universal gas constant, and T_0 is the temperature at which molecular mobility, necessary for crystallization, ceases in the fully dried fibroin. The data of $G \sim K^{1/n}$ were fitted using a Nelder–Mead simplex direct-search routine[47] and the best-fit results to eq 10 are as follows: $G_0 = 4.95\ s^{-1}$, $U = 269$ cal/mol-K, $T_0 = 441$ K (168 °C), shown in Figure 7 by the fitted line. The deduced value of T_0 is below the glass transition temperature of 178 °C, and just slightly below the first onset of the glass transition relaxation process, 170 °C determined from TMDSC.

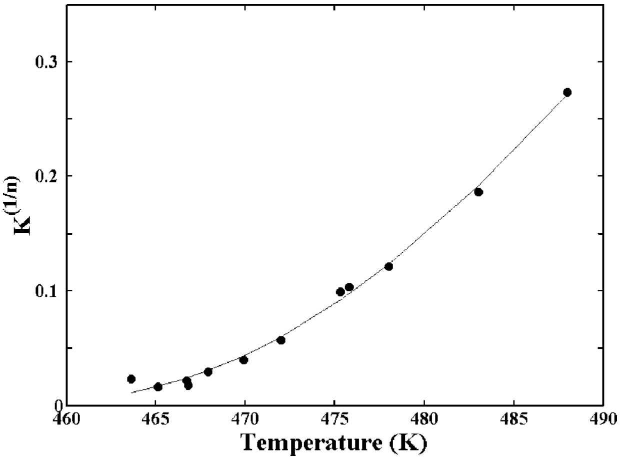

Figure 7. Kinetic data of silk fibroin, $G \sim K^{1/n}$ vs temperature, from combined DSC/FTIR (190 °C < T_c < 205 °C) and X-ray/FTIR studies ($T_c \geq 205$ °C). The line represents the best fit to a transport model, $G = G_0 \exp[-(U/R)/(T - T_0)]$, with best fit parameters of activation energy, $U = 0.269$ kcal/mol-K, and temperature, $T_0 = 441$ K.

Morphology Studies by SEM. SEM was used to observe the structural change in appearance of the fracture surface of silk fibroin protein. Film samples crystallized isothermally at different temperatures with different crystallization times were compared and structure was analyzed in the cross sections. All films had a thickness around 10–20 μm. Figure 8a shows a noncrystalline silk fibroin sample without stacked β-sheet crystals before heat treatment. At a relatively low magnification, silk fibroin protein is comprised of many large pieces of overlapping layers, showing evidence of plastic deformation. At a higher magnification (Figure 8b), the layer is revealed to consist of many bundles with a diameter around 25 ± 5 nm. These bundles contain α helix and random coil chains as indicated by the FTIR spectrum.[22-24] However, these structures are water-soluble and therefore silk noncrystalline materials tend to have weak mechanical properties.

The sample was then isothermally heated at 199 °C for 20 min in the hot stage, and many fibrillar-like structures appeared on the surface of the cross section (Figure 8c,d). The fibrillar structures have an average diameter of 8.5 ± 3 nm. In this sample, the crystallinity is 0.21, from FTIR and TMDSC heat capacity method.[22] Naik et al. [16] measured the size of β-sheet crystals in silk fibroin fibers. Compared with the calculation from WAXS (10.8nm),[16] the major length of the β-sheet crystals obtained from low voltage transmission electron microscopy (LVTEM) was found to be 13.0nm ± 11.9nm. The (GAGAGS)$_n$ lengths in fibroin heavy chain give a size of 11.5 ± 7.4 nm. Therefore, the size of the fibrillar structure in our figures fits well to their experimental data and could be tentatively considered to be the β-sheet regions. With longer heating time at 199 °C, the same sample isothermally crystallized for 90 min was observed and shown in Figure 8e,f. It is clear that not only the size but also the density of the β-sheet crystal domains in the sample increased compared with Figure 8c,d. A high magnification (Figure 8f) shows the diameter of the fibrillar crystals has increased to 15 ± 5 nm. A micelle-like structure finally formed, and became a continuous network. This phenomenon could be used to explain why the silk fibroin sample becomes completely insoluble in aqueous solution after only a little crystallization. Although the sample may still contain large amounts of noncrystalline material inside, their inner structures

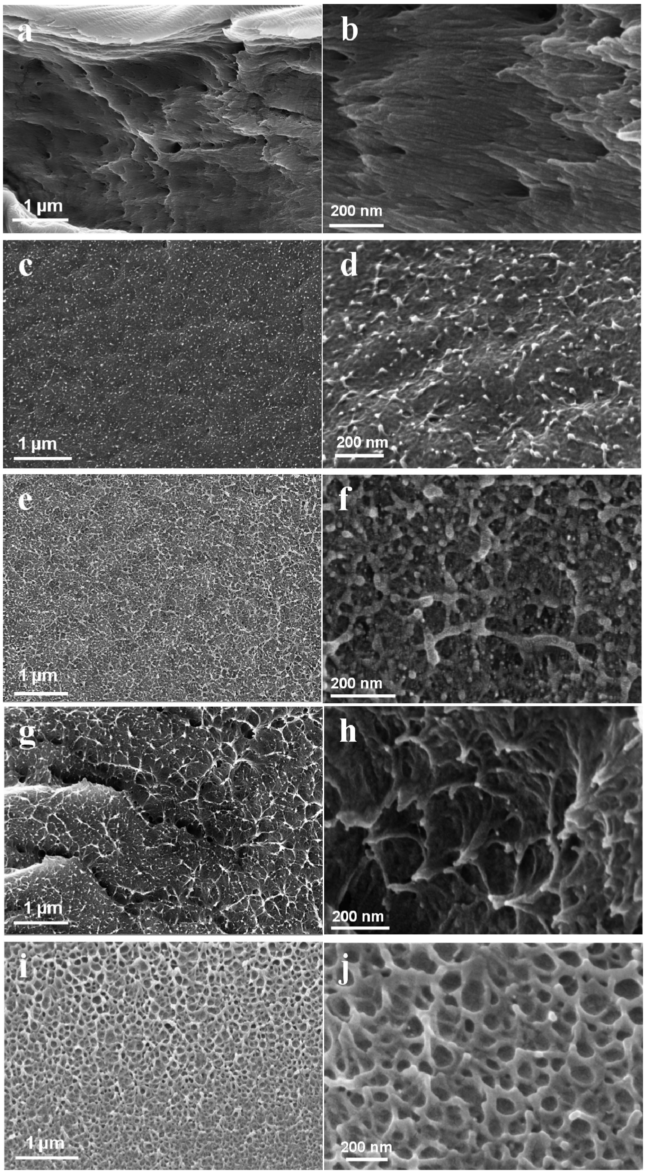

Figure 8. SEM observation of cross sections of silk fibroin films fractured in liquid nitrogen. Noncrystallized sample, before heating treatment (a, b). Sample isothermally heated at 199 °C for 20 min (c, d) and for 60min (e, f). Sample treated by methanol solvent exposure for 3 days (g, h). The edge part of sample crystallized at 199 °C for 90 min and then exposed for 24 h to chymotrypsin enzyme treatment (i, j).

have become a dense united network with the help of the β-sheet crystals, and therefore, the single bundle can not separate from other bundles and cannot freely dissolve in the water.

As a comparison, the noncrystalline silk fibroin sample was also treated by methanol solvent for 3 days. The MeOH-treatments induce the largest β-sheet crystallinity in silk fibroin. Our previous work[22−24] has reported about 0.53−0.56 crystal fraction is formed after 3 days of treatment, which is close to the full percentage of the crystallizable amino-acid domains in silk fibroin. Therefore, the MeOH treated sample can become a model for the fully crystallized silk fibroin. Figure 8g,h shows the SEM cross section of the MeOH treated sample. Compared with the thermally crystallized sample (Figure 8e,f), the MeOH induced crystal domains were larger but less homogenously distributed. A close observation (Figure 8h) shows the β-sheet crystals have the same morphology as that in isothermally crystallized samples. The crystal bundle has an average diameter of 18 ± 5 nm, which is a little thicker than the 199 °C, 60 min treated samples.

To examine the crystalline and noncrystalline structure in the crystallized silk fibroin films, the 199 °C, 90 min isothermally crystallized sample was treated in a chymotrypsin PBS solution. Chymotrypsin has been widely used to biodegrade the noncrystalline regions of fibroin fibers to obtain highly crystalline fibroin protein structure.[61,62] Previous studies have shown that the β-sheet crystals can endure for much longer time than the noncrystalline part during chymotrypsin enzymatic degradation.[61,62] A fracture cross section surface was then obtained in liquid nitrogen and observed by SEM, as shown in Figure 8i,j. The edge of the silk samples was attacked by the enzyme and many holes appeared among the remaining scaffold structures after 24 h enzymatic biodegradation. The remaining scaffolds were similar to the fibrillar structures appearing in Figure 8c−h, and were stable after enzyme treatment. The sample was then examined by FTIR, and a sharp β-sheet crystal peak was observed at 1621 cm^{-1} of the Amide I region. Compared with the final crystallized silk, the chymotrypsin treated sample lost much of its noncrystalline components. Prior to enzymatic degradation, the fibroin contained the following fractions: 0.30 β-sheets, 0.35 turns, 0.32 α-helices/random coils and ~0.03 side chains.[22] After degradation, the β-sheet crystallinity increased to 0.74 ± 0.02, while turns and α-helices/random coils decreased to 0.16 ± 0.02 and 0.09 ± 0.01, respectively, and side chain fraction was about 0.01. When the time of enzymatic degradation was increased to 60 h, the β-sheet crystallinity of the remaining portions increased to 0.85 ± 0.02. (Longer enzyme treatment caused break-up of the sample, and none could be recovered for analysis.) Therefore, we can confirm that the remaining fibrillar-like scaffolds in Figure 8i,j are mainly the β-sheet crystal domains, which formed during the thermal crystallization, but were microphase-separated from the uncrystallizable domains (digested by chymotrypsin and shown as holes in Figure 8i,j).

Discussion

The dimension reduction in crystal growth was first discussed in liquid crystalline polymers because of their special geometry. Fatou et al. [49] studied poly(decamethylene-4,4′-diphenoxy terephthalate) (PDDPT) liquid crystals, and an Avrami exponent $n = 2$ was obtained for the isotropic-mesogenic transformation. Another example is the liquid crystalline rigid rod, wholly aromatic copolyester: a two-dimensional crystal growth is also found when the sample has a special molecular weight distribution.[50] In polymer blend materials the crystallization kinetics tend to be more complicated and Avrami exponents can easily change when the crystal mechanism transforms from confined crystallization to breakout crystallization with a change of crystallization temperature (T_c). A good example is poly(oxyethylene)-*b*-poly(oxybutylene)/ poly(oxybutylene) (E-B/B) blends.[38] Blend polymer materials such as poly(ethylene oxide) (PEO) blended with PMMA, EMMA, or SHS can also form different crystal morphology, as determined in X-ray kinetics study.[42] A recent complicated case is the (nanocomposite) polyethylene (PHDPE) blend with low amount of carbon nanotubes (CNT).[51] An Avrami exponent of approximately 2 indicates a two-dimensional structure was formed in this mixed system. A similar model could also be found in the natural polymer poly(3-D-hydroxybutyrate) (PHB).[33] With an Avrami exponent of $n = 2$, PHB was considered to have a 2-D growth crystallization.

However, the largest group of this type of special crystallization in pure polymer materials was found in block copolymers. Floudas et al. [52] investigated the block copolymers of polystyrene, poly(ethylene oxide), and poly(ϵ-caprolactone) (PS-

PEO-PCL). They found that all their copolymers have a value of n close to 2 during crystallization, which implies a planar disk-like crystal growth from heterogeneous nuclei in this copolymer system, even with different fractions. Superstructures like spherulites and axialites were both observed in the 2-D plane. A similar case also occurred in the poly(ϵ-caprolactone−ethylene glycol) (PCL-PEG) block copolymers with different architectures.[53] A value of $n = 2$ is correlated to a model in which PEG blocks will form a two-dimensional lamellar structure on the growth faces of the formed PCL spherulite crystals in the PEG crystallization temperature region. Müller and Hamley's group recently studied poly(L-lactide)-*b*-poly(ϵ-caprolactone) (PLLA-*b*-PCL) and the poly(p-dioxanone)-*b*-poly(ϵ-caprolactone) (PLPDX-*b*-CL)) diblock copolymers.[54,55] They found that in both copolymer systems, the dimensionality of the PCL block crystal growth could be decreased into two dimensions, which results in an Avrami exponent $n = 2$. The PLLA or PPDX blocks will previously form spherulites and nucleate the PCL blocks in their copolymers. Therefore, the PCL blocks have to crystallize within the amorphous lamellar spaces of the pre-existing PLLA or PPDX spherulites. This limitation causes the crystal growth of the PCL block to be unable to spread into 3-D spaces. All these studies revealed that a dimensionality reduction, or spatial limitation, in the crystal growth can easily occur in amorphous−crystalline block copolymers. Some crystallizable blocks in the copolymer have to self-organize in the small microdomains and the size and morphology of crystals was then strongly driven by these separated microphases.[46,48,54,56−60]

Crystallizable protein structures are essentially similar to the block copolymer structures. Fibroin proteins, like silk fibroin, have been shown to have many repeating crystallizable amino acid blocks or domains, combined with the uncrystallizable domains. The complete sequence of *B. mori* silk fibroin gene shows this protein has 12 repeating regions, mixed with 11 nonrepetitive less ordered regions, in its heavy chain component.[11,17,19] The repetitive region is mainly comprised of the highly repetitive GAGAGS hexamer and less repetitive GAGAGY sequence, which will form β-sheet crystals during protein crystallization. The less ordered blocks, which included hydrophilic and aromatic amino acid residues, can never form β-sheet crystals under any conditions. The nature of the amorphous−crystalline block protein model will fundamentally affect their crystallization kinetics. Moreover, formation of a disorder−order mesophase precursor was also found in our recent studies in silk fibroin protein.[24] With the help of bound water in the protein structure, silk fibroin chains tend to rearrange to become a more ordered and denser precursor structure at around 80 °C in the plasticized material, during heating, before reaching the glass transition temperature of the fully dried silk fibroin ($T_g = 178$ °C). This ordered noncrystalline structure was believed to be related to silk I structure, which is the ordered silk structure within the gland of the silkworm before it spins silk fibers.

Protein Crystallization Kinetics Model. Considering its block copolymer-like crystallization property, we can therefore model the crystallization process of silk fibroin protein (in Figure 9) as follows. The structure of silk fibroin protein in the noncrystalline state has two components: the uncrystallizable chain blocks (dashed lines) mainly include the light chain and the nonrepetitive less ordered regions of the heavy chain in silk fibroin; and the crystallizable blocks (solid lines) mainly containing $(GAGAGS)_n$ amino acid domains (Figure 9a). The crystallizable domains are always separated by the uncrystallizable domains according to the natural amino acid sequence of silk fibroin protein. After the removal of bound water above 80 °C, precursor structures formed in the crystallizable blocks (discussed previously[24]), and these may be the nuclei for subsequent crystal growth. During crystallization above T_g of the dried silk, microphase separation occurs for the crystallizable and uncrystallizable domains (Figure 9b). During isothermal crystallization, strong hydrogen bonds are formed leading to formation of the β-sheet crystals located within their phase-separated domains (Figure 9c). Due to the microphase separation, the growth of the β-sheets crystals is limited to occur only within its microphase space. In order to form crystals, the crystallizable blocks must become associated with each other (*i.e.*, they must become microphase separated from the noncrystallizable blocks). However, we can not tell at what point in the crystallization the microphase separation occurs. The sequence presented in Figure 9b and 9c could just as well be viewed as occurring closely together in time.

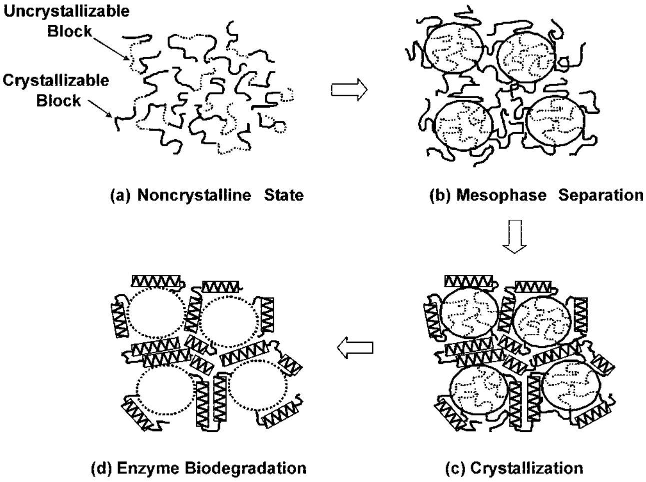

Figure 9. Crystallization kinetics model of silk fibroin protein: (a) noncrystalline silk fibroin chains contain two components, the noncrystallizable blocks (dashed lines) and the crystallizable blocks (solid lines); (b) microphase separation of the crystallizable and noncrystallizable domains occurs; (c) during isothermal crystallization, β-sheet crystals are formed within the crystallizable regions, but are limited in their microphase space, resulting in a crystallization dimensionality reduction; (d) through chymotrypsin enzymatic biodegradation, the noncrystallizable regions of fibroin biodegraded and left behind a scaffold of β-sheet crystalline region within the protein structure.

According to the block copolymer literature, microphase separation results in a limitation of available space for crystal growth, which results in the reduced Avrami exponent $n \sim 2$ (relative to $n \sim 3$ typically seen in synthetic homopolymer spherulitic crystallization), and has been observed in many synthetic block copolymers. Formation of micellar structures in the dried silk,[15] the SEM morphology after enzyme degradation shown in this study, and the LVTEM study,[16] all indicate this phase separation is occurring in silk fibroin. However, this study does not permit the determination of when the microphase separation occurs. It is probable that this is a continuing process throughout the crystallization. The network formed by the crystal structure induces the insolubility of the final silk fibroin structure. After the protein is treated by selected enzyme attack with chymotrypsin the uncrystallizable regions biodegrade and leave behind the more resistant scaffold of crystallized β-sheet crystal regions (Figure 9d).

Conclusions

The crystallization kinetics of the self-assembled β-sheet crystals in multiblock silk fibroin protein were analyzed for the first time. DSC, real-time WAXS and real-time FTIR methods were selected to test the crystallization kinetics data for both low and high temperature regimes. Results show a strong repeatability for the kinetics data obtained from these different experimental methods, and indicate an Avrami exponent of n

~ 2. The morphology observed by scanning electron microscopy after enzymatic degradation is suggestive of microphase separation of the crystallizable and uncrystallizable blocks. A crystallization kinetics model for the β-sheet crystal was then built to explain this special crystallization mechanism in silk fibroin protein. The unique repeating amino acid sequence arrangement in the natural silk protein structure is very similar to many amorphous-crystalline block copolymers, in which crystallizable blocks are covalently bonded with uncrystallizable blocks. This property causes the β-sheet crystallization of silk proteins to be spatially limited during crystal growth, as microphase separation occurs between these regions. Considering the similarity among the naturally occurring multiblock protein structures, this property could be widely applicable in the crystallization of other fibrous proteins.

Acknowledgment. The authors thank the National Science Foundation for support of this research through the Division of Materials Research, Polymers Program, Grant DMR-0402849; the Division of Chemical, Bioengineering, Environmental, and Transport Systems, Grant CBET-0828028; and the MRI Program under DMR-0520655 for thermal analysis instrumentation.

References and Notes

(1) Wunderlich, B., *Macromolecular Physics, Vol. 2, Crystal Nucleation, Growth, Annealing*. Academic Press: New York, 1976.
(2) Schultz, J. M., *Polymer Crystallization: The Development of Crystalline Order in Thermoplastic Polymers*; Oxford University Press: New York, 2001.
(3) Di Lorenzo, M. L.; Silvestre, C. *Prog. Polym. Sci.* **1999**, *24*, 917–950.
(4) Long, Y.; Shanks, R. A.; Stachurski, Z. H. *Prog. Polym. Sci.* **1995**, *20*, 651–701.
(5) Piorkowska, E.; Galeski, A.; Haudin, J. M. *Prog. Polym. Sci.* **2006**, *31*, 549–575.
(6) Yang, J.; McCoy, B. J.; Madras, G. *J. Chem. Phys.* **2005**, *122*, 064901.
(7) De Santis, F.; Adamovsky, S.; Titomanlio, G.; Schick, C. *Macromolecules* **2007**, *40* (25), 9026–9031.
(8) Avrami, M. *J. Chem. Phys.* **1939**, *7*, 1103–1112.
(9) Avrami, M. *J. Chem. Phys.* **1940**, *8*, 212–224.
(10) Avrami, M. *J. Chem. Phys.* **1941**, *9*, 177–184.
(11) McGrath, K., Kaplan, D.; Eds. *Protein-Based Materials*; Birkhauser Press: Boston, MA, 1996; p103−133.
(12) Wang, T.; Wade, R. C. *Journal of Chemical Theory and Computation* **2007**, *3*, 1476–1483.
(13) Day, R.; Bennion, B. J.; Ham, S.; Daggett, V. *J. Mol. Biol.* **2002**, *322* (1), 189–203.
(14) Sham, Y. Y.; Ma, B. Y.; Tsai, C. J.; Nussinov, R. *Proteins-Struct. Funct. Genetics* **2002**, *46*, 308–320.
(15) Jin, H. J.; Kaplan, D. L. *Nature* **2003**, *424* (6952), 1057–1061.
(16) Drummy, L. F.; Farmer, B. L.; Naik, R. R. *Soft Matter* **2007**, *3*, 877–882.
(17) Ha, S. W.; Gracz, H. S.; Tonelli, A. E.; Hudson, S. M. *Biomacromolecules* **2005**, *6*, 2563–2569.
(18) Altman, G. H.; Diaz, F.; Jakuba, C.; Calabro, T.; Horan, R. L.; Chen, J. S.; Lu, H.; Richmond, J.; Kaplan, D. L. *Biomaterials* **2003**, *24*, 401–416.
(19) Foo, C. W. P.; Kaplan, D. L. *Adv. Drug Delivery Rev.* **2002**, *54*, 1131–1143.
(20) Wang, X. Y.; Hu, X.; Daley, A.; Rabotyagova, O.; Cebe, P.; Kaplan, D. L. *J. Controlled Release* **2007**, *121* (3), 190–199.
(21) Wang, X.; Wenk, E.; Hu, X.; Castro, G. R.; Meinel, L.; Wang, X.; Li, C.; Merkle, H.; Kaplan, D. L. *Biomaterials* **2007**, *28*, 4161–4169.
(22) Hu, X.; Kaplan, D.; Cebe, P. *Macromolecules* **2006**, *39*, 6161–6170.
(23) Hu, X.; Kaplan, D.; Cebe, P. *Thermochim. Acta* **2007**, *461* (1−2), 137–144.
(24) Hu, X.; Kaplan, D.; Cebe, P. *Macromolecules* **2008**, *41*, 3939–3948.
(25) Pyda, M.; Hu, X.; Cebe, P. *Macromolecules* **2008**, *41*, 4786–4793.
(26) Chen, H.; Hu, X.; Cebe, P. *J. Thermal Anal. Calorim.* **2008**, *93* (1), 201–206.
(27) Schmidtke, J.; Strobl, G.; ThurnAlbrecht, T. *Macromolecules* **1997**, *30*, 5804–5821.
(28) Strobl, G. *Eur. Phys. J. E* **2000**, *3* (2), 165–183.
(29) Xu, H.; Cebe, P. *Macromolecules* **2005**, *38*, 770–779.
(30) Xu, H.; Cebe, P. *Macromolecules* **2004**, *37*, 2797–2806.
(31) Balta-Calleja, F. J.; Vonk, C. G., *X-ray Scattering of Synthetic Polymers*. Elsevier: Amsterdam, 1989.
(32) Barth, A.; Zscherp, C. *Q. Rev. Biophys.* **2002**, *35*, 369–430.
(33) Hu, Y.; Zhang, J. M.; Sato, H.; Futami, Y.; Noda, I.; Ozaki, Y. *Macromolecules* **2006**, *39*, 3841–3847.
(34) Wang, Y. X.; Bazuin, C. G.; Pezolet, M. *Macromolecules* **2001**, *34*, 6344–6352.
(35) Egan, T. J.; Mavuso, W. W.; Ncokazi, K. K. *Biochemistry* **2001**, *40*, 204–213.
(36) Chen, X.; Shao, Z. Z.; Marinkovic, N. S.; Miller, L. M.; Zhou, P.; Chance, M. R. *Biophys. Chem.* **2001**, *89* (1), 25–34.
(37) Chen, X.; Knight, D. P.; Shao, Z. Z.; Vollrath, F. *Biochemistry* **2002**, *41*, 14944–14950.
(38) Xu, J. T.; Fairclough, J. P. A.; Mai, S. M.; Ryan, A. J.; Chaibundit, C. *Macromolecules* **2002**, *35*, 6937–6945.
(39) Choi, J.; Kwak, S. Y. *Macromolecules* **2004**, *37*, 3745–3754.
(40) Shen, Y.; Johnson, M. A.; Martin, D. C. *Macromolecules* **1998**, *31*, 8857–8864.
(41) Wang, Z. G.; Hsiao, B. S.; Sirota, E. B.; Agarwal, P.; Srinivas, S. *Macromolecules* **2000**, *33*, 978–989.
(42) Lisowski, M. S.; Liu, Q.; Cho, J. D.; Runt, J.; Yeh, F. J.; Hsiao, B. S. *Macromolecules* **2000**, *33*, 4842–4849.
(43) Li, L. B.; de Jeu, W. H. *Macromolecules* **2004**, *37*, 5646–5652.
(44) Trabbic, K. A.; Yager, P. *Macromolecules* **1998**, *31*, 462–471.
(45) Krejchi, M. T.; Cooper, S. J.; Deguchi, Y.; Atkins, E. D. T.; Fournier, M. J.; Mason, T. L.; Tirrell, D. A. *Macromolecules* **1997**, *30*, 5012–5024.
(46) Lorenzo, A. T.; Arnal, M. L.; Muller, A. J.; Boschetti-de-Fierro, A.; Abetz, V. *Macromolecules* **2007**, *40*, 5023–5037.
(47) *Matlab Reference Guide*; The Math Works: Natick, MA, 1992; p 208.
(48) Chen, H. L.; Wu, J. C.; Lin, T. L.; Lin, J. S. *Macromolecules* **2001**, *34*, 6936–6944.
(49) Campoy, I.; Marco, C.; Gomez, M. A.; Fatou, J. G. *Macromolecules* **1992**, *25*, 4392–4398.
(50) Dainelli, D.; Chapoy, L. L. *Macromolecules* **1993**, *26*, 385–390.
(51) Trujillo, M.; Arnal, M. L.; Mueller, A. J.; Bredeau, S.; Bonduel, D.; Dubois, P.; Hamley, I. W.; Castelletto, V. *Macromolecules* **2008**, *41*, 2087–2095.
(52) Floudas, G.; Reiter, G.; Lambert, O.; Dumas, P. *Macromolecules* **1998**, *31*, 7279–7290.
(53) Bogdanov, B.; Vidts, A.; Schacht, E.; Berghmans, H. *Macromolecules* **1999**, *32*, 726–731.
(54) Albuerne, J.; Marquez, L.; Muller, A. J.; Raquez, J. M.; Degee, P.; Dubois, P.; Castelletto, V.; Hamley, I. W. *Macromolecules* **2003**, *36*, 1633–1644.
(55) Hamley, I. W.; Castelletto, V.; Castillo, R. V.; Muller, A. J.; Martin, C. M.; Pollet, E.; Dubois, P. *Macromolecules* **2005**, *38*, 463–472.
(56) Balsamo, V.; de Navarro, C. U.; Gil, G. *Macromolecules* **2003**, *36*, 4507–4514.
(57) Ho, R. M.; Chiang, Y. W.; Lin, C. C.; Huang, B. H. *Macromolecules* **2005**, *38*, 4769–4779.
(58) Shiomi, T.; Takeshita, H.; Kawaguchi, H.; Nagai, M.; Takenaka, K.; Miya, M. *Macromolecules* **2002**, *35*, 8056–8065.
(59) Castillo, R. V.; Arnal, M. L.; Muller, A. J.; Hamley, I. W.; Castelletto, V.; Schmalz, H.; Abetz, V. *Macromolecules* **2008**, *41*, 879–889.
(60) Loo, Y. L.; Register, R. A.; Ryan, A. J. *Macromolecules* **2002**, *35*, 2365–2374.
(61) Li, M. Z.; Ogiso, M.; Minoura, N. *Biomaterials* **2003**, *24*, 357–365.
(62) Arai, T.; Freddi, G.; Innocenti, R.; Tsukada, M. *J. Appl. Polym. Sci.* **2004**, *91*, 2383–2390.
(63) Sinsawat, A.; Putthanarat, S.; Magoshi, Y.; Pachter, R.; Eby, R. K. *Polymer* **2002**, *43*, 1323–1330.

MA802481P